ACS Catalysis

Research Article

Cite This: ACS Catal. 2019, 9, 10761−10772

pubs.acs.org/acscatalysis

Cu(II) Ions Induced Structural Transformation of Cobalt Selenides for Remarkable Enhancement in Oxygen/Hydrogen Electrocatalysis

Jiale Dai,[†,○] Dengke Zhao,[†,○] Wenming Sun,[‡,○] Xiaojing Zhu,[†] Li-Jun Ma,[§] Zexing Wu,[∥] Chenghao Yang,[†] Zhiming Cui,[⊥] Ligui Li,[*,†,#] and Shaowei Chen[†,▽]

[†]Guangzhou Key Laboratory for Surface Chemistry of Energy Materials, New Energy Research Institute, College of Environment and Energy, South China University of Technology, Guangzhou 510006, China

[‡]College of Science, China Agricultural University, Beijing 100193, China

[§]Key Laboratory of Theoretical Chemistry of Environment Ministry of Education, School of Chemistry and Environment, South China Normal University, Shipai, Guangzhou 510631, China

[∥]State Key Laboratory Base of Eco-chemical Engineering, College of Chemistry and Molecular Engineering, Qingdao University of Science & Technology, 53 Zhengzhou Road, Qingdao 266042, China

[⊥]The Key Laboratory of Fuel Cell Technology of Guangdong Province, School of Chemistry and Chemical Engineering, South China University of Technology, Guangzhou 510641, China

[#]State Key Laboratory of Polymer Physics and Chemistry, Changchun Institute of Applied Chemistry, Chinese Academy of Sciences, Changchun 130022, China

[▽]Department of Chemistry and Biochemistry, University of California, 1156 High Street, Santa Cruz, California 95064, United States

Supporting Information

ABSTRACT: Efficient nonprecious multifunctional catalysts are indispensable to enable the widespread applications of several important electrochemical energy technologies. Herein, catalytically active metastable monoclinic-phase Co_3Se_4 nanorods supported on carbon hybrids of reduced graphene oxide and carbon nanotubes (Cu-14-Co_3Se_4/GC) were selectively prepared by adding Cu(II) ions to the precursors that were successively treated by a hydrothermal process and thermal annealing at 300 °C, while only low-activity orthorhombic-phase $CoSe_2$ nanorods were obtained without the addition of Cu(II) ions. The resulting grape-bunch-like Cu-14-Co_3Se_4/GC sample contained a trace amount of Cu element and showed efficient trifunctional activities, with an oxygen evolution reaction (OER) overpotential of 280 mV and impressively the highest half-wave potential of +0.782 V (i.e., $E_{ORR,1/2}$) for the oxygen reduction reaction (ORR) in 0.1 M KOH as well as the lowest hydrogen evolution reaction (HER) overpotential of 166 mV among the Co_3Se_4 composites reported to date at 10 mA cm^{-2} in 1.0 M KOH. Moreover, a voltage difference (ΔE) of only 0.680 V was observed between the potential for OER at 10 mA cm^{-2} ($E_{OER,10}$) and $E_{ORR,1/2}$ in 1.0 M KOH, and merely 1.620 V was required to reach 10 mA cm^{-2} in overall water splitting. X-ray photoelectron spectroscopy measurements and theoretical simulations reveal the evident change of the electronic state after incorporation of Cu atoms onto Co−Se skeletons. Density functional theory calculations suggest that upon structural transformation from orthorhombic $CoSe_2$ to monoclinic Co_3Se_4, the Gibbs free energies of the rate-determining steps were significantly reduced from 0.43 to −0.22 eV for ORR, from 2.64 to 1.90 eV for OER, and from 1.08 to 0.23 eV for HER, mainly accounting for the high catalytic activities of Cu-14-Co_3Se_4/GC. Besides, the presence of abundant open-channel nanocavities in three-dimensional grape-bunch-like Cu-14-Co_3Se_4/GC helps maximize the exposure of active sites and facilitates mass diffusion, while the GC networks improve electrical conductivity, hence expediting the electrocatalysis process. The results in the present work highlight the importance of structural engineering in electrocatalysis and may pave an avenue for the preparation of low-cost, efficient, and multifunctional electrocatalysts.

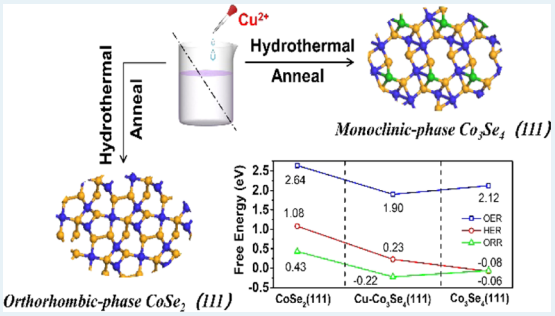

KEYWORDS: *cobalt selenide, multifunctional electrocatalyst, oxygen reversible electrocatalysis, hydrogen evolution reaction, structural transformation*

INTRODUCTION

Metal−air batteries and water electrolyzer represent two important electrochemical energy conversion and storage

Received: September 21, 2019
Revised: October 16, 2019
Published: October 17, 2019

Downloaded via UNIV OF CALIFORNIA SANTA CRUZ on December 18, 2019 at 00:32:55 (UTC).
See https://pubs.acs.org/sharingguidelines for options on how to legitimately share published articles.

© 2019 American Chemical Society

DOI: 10.1021/acscatal.9b04060
ACS Catal. 2019, 9, 10761−10772

systems, which concurrently entail multiple reactions during operation. For example, metal−air batteries entail oxygen reduction reaction (ORR) during discharging, while in the charging state, a reversible process of ORR, that is, oxygen evolution reaction (OER), proceeds at the same electrode.[1−6] As for full water-splitting systems, they concurrently entail OER and hydrogen evolution reaction (HER) at the anode and cathode, respectively.[7] In some combinative systems, such as using a Zn-air battery to implement water splitting, the aforementioned three reactions are involved at the same time. Normally, Pt-based nanomaterials are considered as state-of-the-art catalysts toward ORR and HER, while Ir-/Ru-based compounds usually serve as the benchmark catalysts for OER. Yet, it remains a challenge to efficiently catalyze the above three reactions in the same working electrolyte with one single commercial electrocatalyst such as the Pt-based nanomaterials or nanostructured Ir/Ru compounds.[8,9] Moreover, the low abundance and high cost of these precious-metal-based nanocatalysts also severely impede their widespread applications.[10−12] Therefore, exploration of novel nonprecious-metal-based electrocatalysts that integrate multifunctional catalytic activities into one catalyst entity can not only help significantly simplify the corresponding device structures and fabrication process[3] but also markedly reduce production cost.[13]

Recently, cobalt selenides have gained increasing research attention due to their considerable oxygen/hydrogen electrocatalytic activities, as well as various advantages, such as low cost, environmental friendliness, and high chemical stability.[14] Thereunto, stoichiometric $CoSe_2$, a well-reported layered cobalt selenide to date, is regarded as a terrific candidate for OER because its $t_{2g}^6e_g^1$ electronic configuration is near the optimal e_g filling,[15,16] and indeed its activities have been experimentally identified in oxygen/hydrogen electrocatalysis.[17−20] However, the basal planes of $CoSe_2$ are not catalytically active at all, which usually makes its catalytic efficiency far below what is expected,[16] similar to the predicaments encountered in other layered transition-metal chalcogenides where very limited defects in basal planes or sites on edges are active[21] in electrocatalysis.

Theoretically, nonlayered structured cobalt selenides should easily display more crystalline facets, as compared with the layered counter ones, and hence can expose more active sites to expedite electrocatalysis. Of these, the typical nonlayered Co_3Se_4 represents an emerging candidate for efficient oxygen/hydrogen electrocatalysis due to its abundant accessible surface active sites, intrinsic half-metallic behavior that renders high electronic conductivity, and the presence of a near-optimal electronic configuration that is similar to $CoSe_2$.[22] However, reports on the synthesis of Co_3Se_4 composites and their catalytic applications remain rather scarce.[23] Besides, efficient ORR activities of Co_3Se_4 have never been reported to the best of our knowledge. Therefore, constructing Co_3Se_4-based catalysts with efficient trifunctional activities toward HER, OER, and ORR in the same working electrolyte is still a challenging work.

In this work, structural transformation from orthorhombic $CoSe_2$ (o-$CoSe_2$) to monoclinic Co_3Se_4 (m-Co_3Se_4) was induced by adding Cu(II) ions to the cobalt precursor. As compared with the low-activity sample o-$CoSe_2$ nanorods supported on carbon hybrids of reduced graphene oxide (GO) and carbon nanotubes (CNT) ($CoSe_2$/GC), the resulting Cu−Co_3Se_4/GC showed dramatic enhancements in the OER, HER, and ORR catalytic activities, featuring an $E_{OER,\ 10}$ of +1.510 V and an $E_{HER,\ 10}$ of −0.166 V in 1.0 M KOH aqueous solution, and a half-wave potential of +0.782 V in 0.1 M KOH aqueous solution. Impressively, the overpotential for HER on Cu-14-Co_3Se_4/GC is the lowest reported to date for Co_3Se_4 composites, and this is the first report on the effective ORR and also trifunctional electrocatalysis with Co_3Se_4-based catalysts (Table S1). X-ray photoelectron spectroscopy (XPS) analysis and theoretical simulations revealed evident change of the electronic state after introducing Cu atoms into Co−Se skeletons. Density functional theory (DFT) calculations suggested that the Gibbs free energies of the rate-determining steps for oxygen and hydrogen electrocatalyses were both drastically reduced after the structural transformation from o-$CoSe_2$ to m-Co_3Se_4, which accounts for the high intrinsic catalytic activities of Co_3Se_4. Besides, the 3D grape-bunch-like morphology is conducive to the mass diffusion, and the included GC networks help improve the electrical conductivity, hence promoting the electrocatalysis process. The results in this work not only demonstrate the importance of structural regulation of cobalt selenides but also open up a novel route for the preparation of low-cost, efficient multifunctional electrocatalysts for correlated electrochemical energy conversion technologies.

EXPERIMENTAL SECTION

Syntheses of GO and CNT. GO nanosheets were synthesized through acid oxidation and exfoliation of graphite powders (Sigma, 800 mesh) according to the method previously reported[24] and subsequently dialyzed with deionized water to form a neutral dispersion with a GO concentration of about 6.7 mg mL^{-1}. CNTs were also treated with the mixture of nitric acid and fuming sulfuric acid and then dialyzed with deionized water to form a neutral dispersion, followed by centrifugation and freeze-drying to obtain the black powder.

Synthesis of Cu-14-Co_3Se_4/GC. Briefly, metal salts containing 1.44 g of $Co(NO_3)_2{\cdot}6H_2O$ and 0.24 g of $Cu(NO_3)_2{\cdot}3H_2O$, 0.04 g of acid-treated CNTs, and 6.00 mL of GO aqueous solution with a concentration of 6.7 mg mL^{-1} were dispersed in 80.00 mL of methanol. Herein, the weight ratio of $Cu(NO_3)_2{\cdot}3H_2O$ to metal salt mixture of $Co(NO_3)_2{\cdot}6H_2O$ and $Cu(NO_3)_2{\cdot}3H_2O$ was calculated to be 14.3%, and the resulting sample was denoted Cu-14-Co_3Se_4/GC.

After sonication for 30 min, 20.00 mL of methanol solution with a dimethylimidazole concentration of 0.20 g mL^{-1} was added under gentle stirring. Subsequently, the mixture was stood at room temperature for 24 h, and the resulting precipitate was collected by centrifugation and washed with ethanol several times, followed by freeze-drying to obtain a violet powder.

Afterward, 0.10 g of violet powder and 0.10 g of Na_2SeO_3 were added into 30.00 mL of DETA aqueous solution (33.33 wt %) under stirring to form a homogeneous solution. Afterward, the homogeneous solution was transferred into a 50.00 mL sealed Teflon-lined autoclave and kept at 150 °C for 12 h and then naturally cooled to room temperature. The solid was collected by centrifugation and washed by ethanol and deionized water several times, followed by freeze-drying. The thus-obtained black powder was then placed in a tubular oven and heated at 300 °C under an Ar atmosphere for 2 h to finally obtain the Cu-14-Co_3Se_4/GC.

For comparison, control samples, such as Cu-11-Co_3Se_4/GC and Cu-21-Co_3Se_4/GC, were also prepared with different weight ratios of $Cu(NO_3)_2{\cdot}3H_2O$ to metal salt mixture of $Co(NO_3)_2{\cdot}6H_2O$ and $Cu(NO_3)_2{\cdot}3H_2O$ in the precursors according to the same method used for synthesis of Cu-14-Co_3Se_4/GC.

DOI: 10.1021/acscatal.9b04060
ACS Catal. 2019, 9, 10761−10772

Scheme 1. Sketch for Showing the Preparation Process of Cu−Co_3Se_4/GC Composites

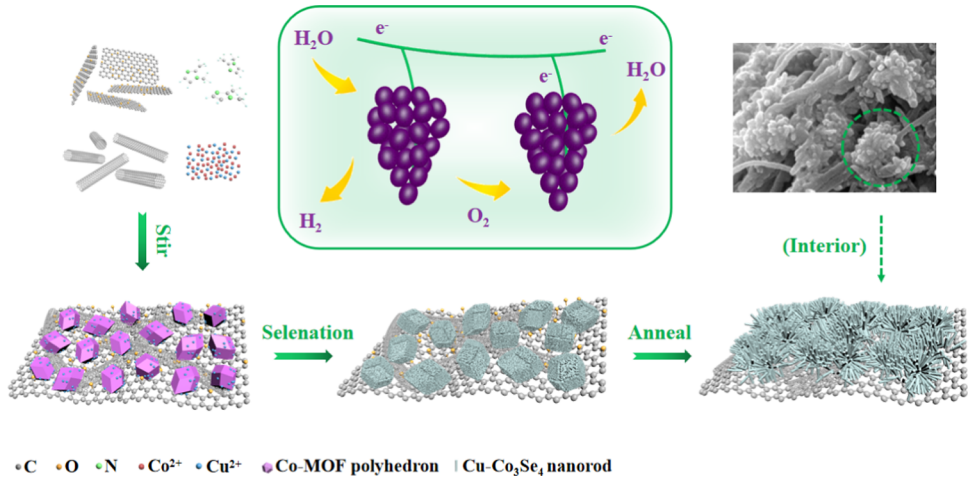

Synthesis of $CoSe_2$/GC. The $CoSe_2$/GC composite was synthesized through a similar process without the addition of $Cu(NO_3)_2{\cdot}3H_2O$.

Synthesis of $CoSe_2$. $CoSe_2$ was also synthesized with a similar process without the addition of GO and CNTs.

Characterizations. Transmission electron microscopy (TEM) measurements were conducted on FEI Tecnai G2 F30 with an acceleration voltage of 300 kV. The TEM samples were prepared by drop-casting a catalyst dispersion directly onto a copper grid coated with a thin holy carbon film. Scanning electron microscopy (SEM) measurements were conducted with a field-emission scanning electron microscope (S-4800, Hitachi). XPS measurements were performed on a Phi X-tool instrument. Powder X-ray diffraction (XRD) patterns were recorded with a Bruker D8-Advance diffractometer using Cu Kα radiation. Brunauer−Emmett−Teller (BET) surface area was determined by N_2 adsorption/desorption at 77 K with a Micromeritics ASAP 2010 instrument according to the Barrett−Joyner−Halenda method.

Electrochemistry. Electrochemical measurements of ORR activity were performed with an electrochemical workstation (CH Instruments, Inc., Model CHI 750E) in a 0.1 M KOH aqueous solution. Rotating ring-disk electrode (RRDE) with a glassy carbon disk and gold ring was used as the working electrode, while an Ag/AgCl electrode (3 M KCl) and a platinum foil were utilized as the reference and counter electrodes, respectively. To prepare catalyst dispersion, 5.0 mg of the investigated catalyst was dispersed in 1.0 mL of ethanol, and the mixture was sonicated for 30 min. Subsequently, 20.0 μL of the catalyst ink along with 10.0 μL of the Nafion solution (5% Nafion in ethanol) was dropcast onto the glassy carbon electrode (GCE) surface at a catalyst loading of 0.510 mg cm^{-2} and finally dried at room temperature.

The number of electron transfer (n) and the yield of H_2O_2 were calculated according to eqs 1 and 2, respectively

$$n = \frac{4I_{disk}}{I_{ring}/N + I_{disk}} \quad (1)$$

$$H_2O_2\% = \frac{200I_{ring}/N}{I_{ring}/N + I_{disk}} \quad (2)$$

where I_{disk} is the disk current, I_{ring} is the ring current, and n is the current collection efficiency (37%) of the rotating ring-disk electrode (RRDE).

OER tests were performed in a 1.0 M KOH aqueous solution with the same electrochemical setup at an identical catalyst loading. HER measurements were conducted with an electrochemical setup that is similar to that of ORR measurements, but the platinum foil counter electrode was replaced by a carbon rod.

Computational Methods. Calculations of the geometrical and electronic properties were implemented in the CASTEP code (Zeitschrift Fuer Kristallographie, 2005, 220, 567−570). The generalized gradient approximation having the Burke−Ernzerhof potential for solids was used. A kinetic energy cutoff of 400 eV and the BFGS optimization method were adopted. During the optimization process, the total energy was designed to converge to 1×10^{-5} eV, and the force per atom was diminished to 0.03 eV $Å^{-1}$. The Brillouin zone of the supercell was sampled by $2 \times 2 \times 1$ and $4 \times 4 \times 1$ uniform k-point meshes in slab geometry optimization and electronic property calculation, respectively. The calculated lattice constants for bulk $CoSe_2$ and Co_3Se_4 are in good agreement with the previous calculation values (Table S2).

Based on our experimental results, $CoSe_2(111)$, $Co_3Se_4(111)$, and Cu-doped $Co_3Se_4(111)$ slab models were adopted to investigate their HER and OER performances. The periodically repeated slabs were separated from their neighboring images by a 12 Å vacuum in the direction perpendicular to the surface. For all slab models, the dipolar correction was included. Computational details of HER and OER are illustrated in the Supporting Information. Spin-polarization was considered in all calculations.

RESULTS AND DISCUSSION

The synthesis process of Cu−Co_3Se_4/GC is depicted in Scheme 1, where the hybrid of GO, CNTs, and Cu-doped Co-containing metal−organic frameworks was used as the precursor. Subsequent hydrothermal treatment in the presence of Na_2SeO_3 promoted the selenylation of cobalt as well as partial reduction of GO. The obtained solid was further annealed in an Ar atmosphere at a low temperature of 300 °C, leading to the formation of Cu-14-Co_3Se_4/GC. Thereunto, the hybrid of GO and CNTs is conducive to electron transfer, while the network of CNTs might help prevent GO from excessive agglomeration and stacking.

DOI: 10.1021/acscatal.9b04060
ACS Catal. 2019, 9, 10761−10772

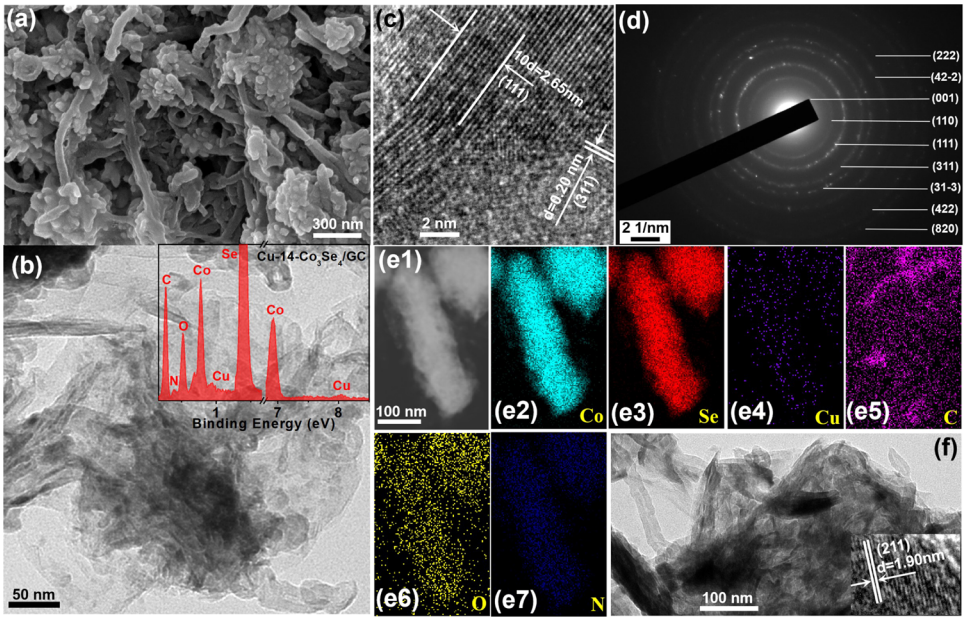

Figure 1. (a) SEM image; (b) TEM images; inset to panel (b) is the EDS spectrum; (c) HR-TEM images of Cu-14-Co_3Se_4/GC. (d) SAED pattern of Cu-14-Co_3Se_4/GC. (e1) High-angle annular dark-field scanning transmission electron microscopy image and the corresponding elemental distribution images for (e2) Co, (e3) Se, (e4) Cu, (e5) C, (e6) O, and (e7) N. (f) TEM image of $CoSe_2$/GC; inset to panel f is an HR-TEM image of $CoSe_2$/GC.

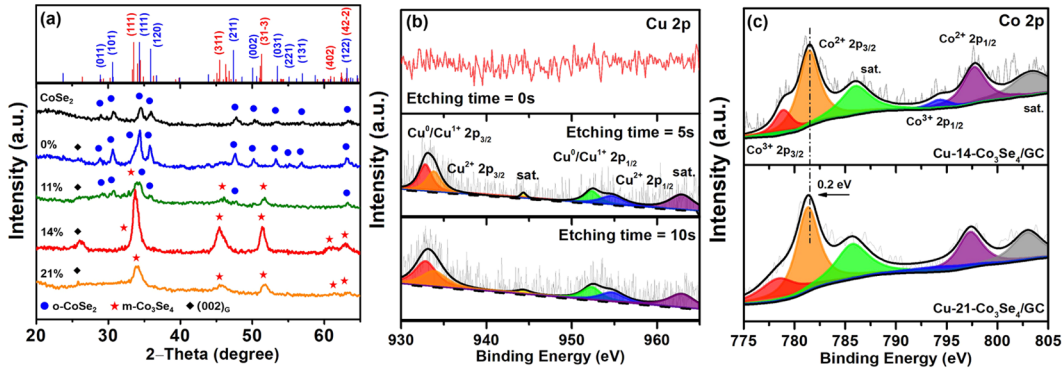

Figure 2. (a) XRD profiles of $CoSe_2$, cobalt selenide/GC composites prepared with 0, 11, 14, and 21 wt % of Cu salt in the precursor. (b) Cu 2p XPS spectra for the Cu-14-Co_3Se_4/GC sample determined at different Ar ion etching times. (c) High-resolution Co 2p XPS spectra of cobalt selenide/GC composites prepared with 14 and 21 wt % of Cu salt in the precursor.

From the SEM image depicted in Figure 1a, one can find that the obtained Cu-14-Co_3Se_4/GC composite shows a morphology resembling grape bunches, where CNTs serve as vines and the abundant nanorods coated by rGO (Figure 1b) as grapes. Moreover, abundant open-channel nanocavities with diameters ranging from several nanometers to about 200 nm are observed (Figure 1a,b), which may promote the mass diffusion process. The corresponding high-resolution TEM (HR-TEM) image (Figure 1c) shows obvious lattice fringes with d-spacings of 0.265 nm and 0.200 nm, corresponding to the (111) and (311) planes of m-Co_3Se_4, respectively. The selected-area electron diffraction (SAED) image (Figure 1d) depicts a series of well-resolved diffraction rings, which can be fully indexed according to the electron diffraction patterns of m-Co_3Se_4. From the series of elemental mapping images of Cu-14-Co_3Se_4/GC (Figure 1e), it is found that the distributions of Co, Se, Cu, and O elements are highly localized and resemble each other, indicative of the successful formation of Cu-doped Co_3Se_4 nanorods. Element contents are measured by an energy-dispersive spectrometer (EDS) (inset to Figure 1b), and one can find that the Se/Co atomic ratios for Cu-14-Co_3Se_4/GC and $CoSe_2$/GC samples are highly close to 4:3 and 2:1 (Table S3), further confirming the formation of Co_3Se_4 and $CoSe_2$ in these two samples, respectively. Besides, the element content of Cu in Co_3Se_4 is determined to be 0.36 atom % (corresponding to about 1.07 wt %), which is also very close to that (~0.88 wt %) determined by inductively coupled plasma atomic emission spectroscopy (ICP-AES). Note that the morphology of Cu-14-Co_3Se_4/GC also resembles $CoSe_2$/GC (Figure 1f), signifying the negligible impacts on the morphology of cobalt selenides upon Cu(II) ion doping. However, from the inset HR-TEM image of $CoSe_2$/GC in panel f, lattice fringes with a d-spacing of 0.190 nm, corresponding to the (211) plane of o-$CoSe_2$, can be well resolved, indicating that indeed the crystallographic phase has been essentially changed after adding Cu(II) ions to the precursor.

The presence of structural transformation is further supported by XRD measurements. As depicted in Figure 2a, the $CoSe_2$/GC

DOI: 10.1021/acscatal.9b04060
ACS Catal. 2019, 9, 10761−10772

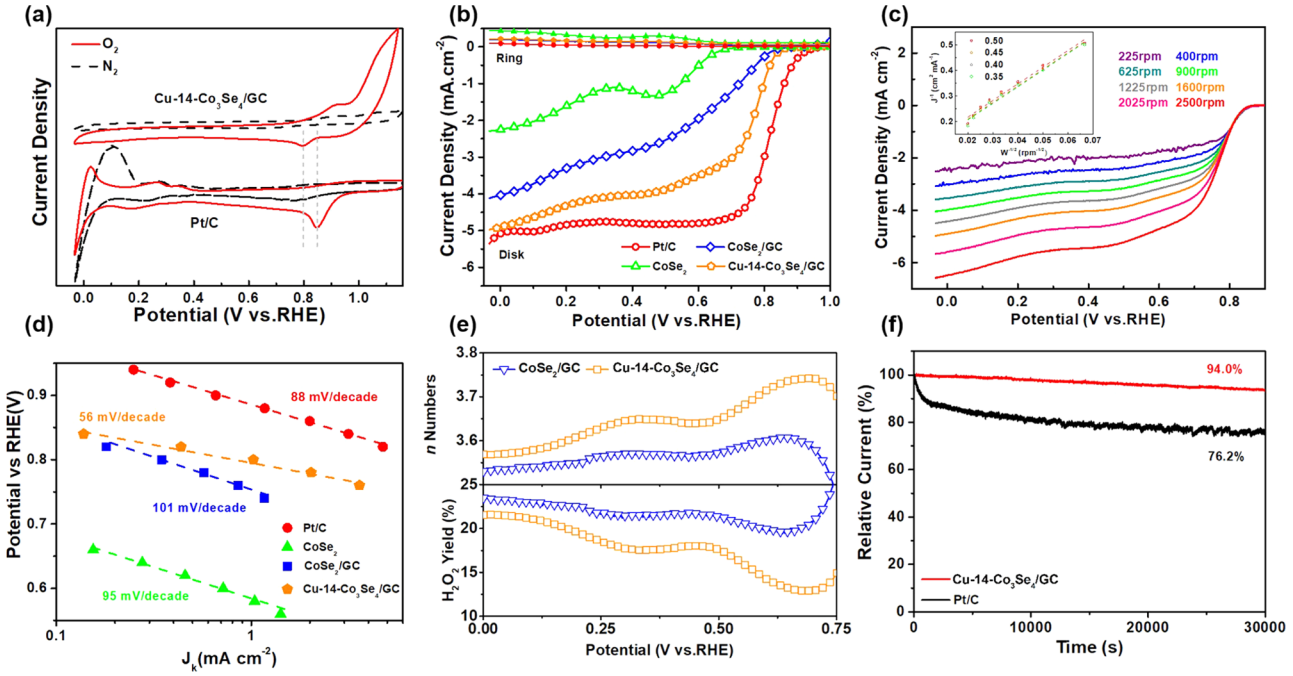

Figure 3. (a) CV curves of Cu-14-Co_3Se_4/GC and commercial Pt/C catalyst (20 wt %) in a 0.1 M KOH solution saturated with N_2 (black dashed line) or O_2 (red solid line) at a scan rate of 10 mV s^{-1}. (b) RRDE voltammograms of Cu-14-Co_3Se_4/GC, $CoSe_2$/GC, $CoSe_2$, and Pt/C catalyst at the electrode rotation rate of 1600 rpm. (c) Linear sweep voltammetry (LSV) curves for Cu-14-Co_3Se_4/GC at the rotation rates of 225−2500 rpm; inset is the corresponding Koutecky−Levich (K−L) plots at different potentials. (d) Corresponding Tafel plots of different catalysts. (e) Number of electron transfers and corresponding H_2O_2 yield of a GCE loaded with Cu-14-Co_3Se_4/GC and $CoSe_2$/GC at an electrode rotation speed of 1600 rpm in O_2-saturated 0.1 M KOH at an electrode rotation rate of 1600 rpm as well as a potential sweep rate of 10 mV s^{-1}. (f) Chronoamperometric curves for Cu-14-Co_3Se_4/GC and Pt/C catalyst determined at +0.500 V in an O_2-saturated 0.1 M KOH aqueous solution at an electrode rotation rate of 900 rpm. The catalyst loadings were 0.510 and 0.255 mg cm^{-2} for the commercial Pt/C catalyst (20 wt %).

sample that was prepared without the addition of Cu(II) ions shows apparent diffraction peaks at 2θ of 26.03, 28.89, 30.65, 34.35, 35.73, 47.55, 50.16, 53.20, 55.06, 56.90, and 63.11°, corresponding to the (002) plane of graphitized carbon and (011), (101), (111), (120), (211), (002), (031), (221), (131), and (122) planes of o-$CoSe_2$ (mp-20862), respectively, indicating the formation of o-$CoSe_2$ composite with carbons. When Cu(II) ions are added to the precursors for the synthesis of cobalt selenide/GC composites, the intensity of XRD peaks attributed to o-$CoSe_2$ (denoted by blue solid circles) gradually decreases on increasing the weight ratio of Cu salt from 0 to 11 wt %. Concurrently, three new peaks (indicated by red solid pentagons) with a 2θ of 33.70, 45.44, and 51.37°, which are attributed to the (111), (311), and (31$\bar{3}$) planes of m-Co_3Se_4 (mp-11800),[10] respectively, arise. Addition of a higher ratio of Cu salt (14 wt %) results in complete disappearance of the XRD peaks of o-$CoSe_2$, along with the appearance of two more new peaks at 2θ of 60.78 and 62.98°, which are attributed to the (402) and (42$\bar{2}$) planes of m-Co_3Se_4. These observations signify the formation of pure m-Co_3Se_4 in the composite of Cu-14-Co_3Se_4/GC. However, further increasing the ratio of Cu salt to 21 wt % causes no obvious change to the XRD profile, as compared with Cu-14-Co_3Se_4/GC in terms of peak number and position, suggesting that the m-Co_3Se_4 phase remains unchanged. Because Cu has a slightly higher electronegativity than Co, that is, 1.90 vs 1.88, respectively, the replacement of partial Co by Cu may cause more Co atoms to coordinate with Se, so that a new equilibrium state of charge distribution is formed between Co and Se sites, finally leading to the change of the stoichiometric ratio between Co and Se in cobalt selenides as well as the corresponding electronic state.[25]

The surface composition of investigated samples was probed by XPS measurements. The signals of Co, Se, C, N, and O elements are resolved in the survey spectra of Cu-14-Co_3Se_4/GC and $CoSe_2$/GC (Figure S1), while no apparent peak can be identified from the Cu 2p XPS spectrum of Cu-14-Co_3Se_4/GC (Figure 2b), probably because the content of the Cu element is too low to reach the detection limit of surface-sensitive XPS analysis due to the shield of the thin GC layer. As expected, after etching with the Ar ion for 5 s, three pairs of Cu 2p XPS peaks appear at 932.9, 952.5, 934.0, 955.1, 944.3, and 963.0 eV, which are ascribed to Cu^0, Cu^+, or Cu^{2+} species and their correlated satellite peaks, respectively.[26,27] On the basis of this XPS analysis, the corresponding Cu elemental content is determined to be 0.40 atom %, which is close to the aforementioned results from EDS and ICP-AES measurements. With a prolonged etching time of 10 s, the Cu 2p XPS spectrum remains nearly unchanged as compared with that obtained with an etching time of 5 s, and an almost identical Cu elemental content of ca. 0.43 atom % is observed.

The Co 2p XPS spectra for Cu−Co_3Se_4/GC samples prepared with 14 and 21 wt % Cu salt addition are shown in Figure 2c, where distinct peaks of Co^{3+} $2p_{3/2}$, Co^{2+} $2p_{3/2}$, Co^{3+} $2p_{1/2}$, and Co^{2+} $2p_{1/2}$ at about 778.9, 781.5, 794.3, and 797.7 eV, respectively, are observed for both samples, signifying the coexistence of Co^{2+} and Co^{3+} species in Co_3Se_4 nanorods.[10,23,28] Besides, the satellite at 803.4 eV indicates the presence of an antibonding orbital between Co and Se atoms, indicative of a near-optimal electronic state that is desired for high-performance electrocatalysts.[16] The satellite peak at ca. 786.0 eV might arise from the hybridization between the Co 3d electrons and Se 4p spin-up (α) electrons,[23] and its appearance suggests a half-

DOI: 10.1021/acscatal.9b04060
ACS Catal. 2019, 9, 10761−10772

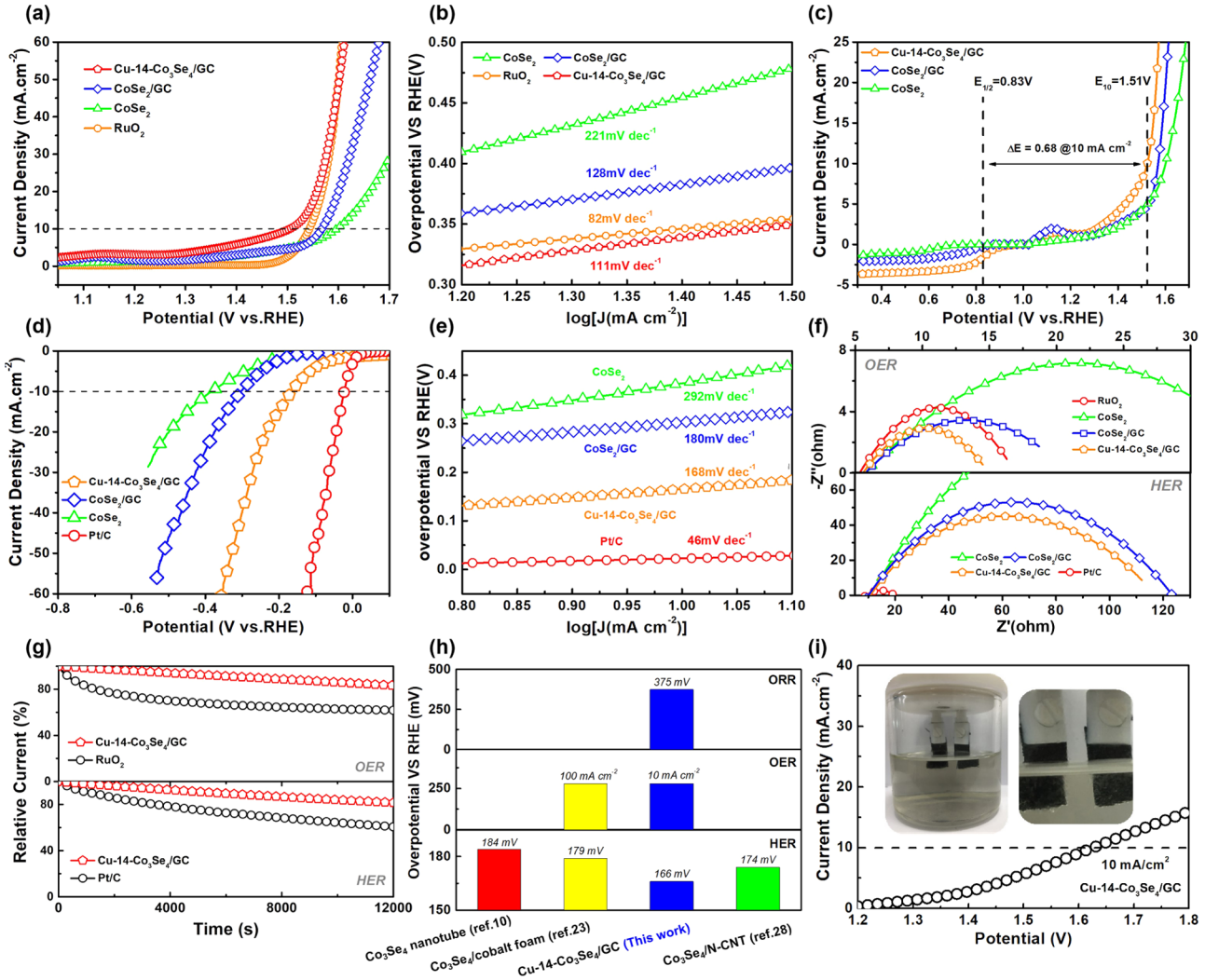

Figure 4. (a) LSV curves; and (b) corresponding Tafel plots of different samples catalyzing OER in 1.0 M KOH solution at a potential scan rate of 10 mV s^{-1} after iR correction. (c) LSV curves of different samples measured in 1.0 M KOH aqueous solution for comparing their bifunctional activities toward both ORR and OER. (d) LSV curves of different samples; and (e) corresponding Tafel plots for samples catalyzing HER in 1.0 M KOH solution at a potential scan rate of 10 mV s^{-1} after iR correction. (f) Electrochemical impedance spectra of different samples measured on a GCE electrode in 1.0 M KOH aqueous solution with a bias of +1.600 V versus RHE during OER catalysis (upper part in panel f) and −0.300 V versus RHE for HER catalysis (bottom part in panel d). All measurements were conducted with an alternating current amplitude of 5 mV in the frequency range of 10 kHz to 0.01 Hz. (g) Chronoamperometric curves detected at an initial current of 10 mA cm^{-2} for different catalysts when catalyzing OER (upper part in panel d) and HER (bottom part in panel d). (h) Diagrams for comparing the ORR, OER, and HER performances of different Co_3Se_4-based electrocatalysts reported in the literature and the present work. (i) LSV curve of full water splitting conducted in 1.0 M KOH aqueous solution at a potential scan rate of 10 mV s^{-1}. Inset to panel i is the optical image for showing a full water-splitting system with Cu-14-Co_3Se_4/GC modified carbon fiber cloth as both a cathode and an anode.

metallic property for Co_3Se_4 that is beneficial to charge transfer. Note that the peak of Co^{2+} $2p_{3/2}$ in phase-pure m-Co_3Se_4 shows a negative shift of about 0.20 eV after the additional amount of Cu salt was further increased from 14% to 21 wt % (Figure 2c), demonstrating that Cu doping can not only induce structural transformation but also affect the electronic structure of m-Co_3Se_4.[27,29,30]

The specific surface area and pore size distribution of the as-synthesized nanocomposites are determined by BET measurements (Figure S3). On the basis of the N_2 adsorption/desorption isotherms, the specific surface area value is calculated to be 66.8 m^2 g^{-1} for Cu-14-Co_3Se_4/GC, which is higher than the 53.5 m^2 g^{-1} for $CoSe_2$/GC and 9.2 m^2 g^{-1} for $CoSe_2$. Besides, these three samples show a type-IV adsorption/desorption isotherm of N_2 at 77 K with an evident hysteresis loop, indicating the presence of mesopores, which is beneficial to the mass diffusion/transfer process.[31,32] From the corresponding pore size distribution plots (Figure S3), the dominant pore diameter is determined to be ca. 2.8 nm for Cu-14-Co_3Se_4/GC and about 4.0 nm for $CoSe_2$/GC and $CoSe_2$.

The ORR catalytic activities for Cu-14-Co_3Se_4/GC are first evaluated by cyclic voltammetry (CV) measurements. As depicted in Figure 3a, the CV curve for Cu-14-Co_3Se_4/GC acquired in a N_2-saturated 0.1 M KOH solution only shows a featureless double-layer charging profile within the potential range of −0.030 to +1.150 V (vs reversible hydrogen electrode (RHE)). As for the CV scans conducted in an O_2-saturated electrolyte solution, the cathodic current shows an obvious peak at about +0.800 V (vs RHE) due to the appearance of oxygen electroreduction, which is slightly lower than that of the

DOI: 10.1021/acscatal.9b04060
ACS Catal. 2019, 9, 10761−10772

commercial Pt/C catalyst and comparable to the electrocatalysts synthesized through the low-temperature pathway in the literature (Table S1).[33−35] The detailed ORR activities of the series catalysts are then studied by a rotating ring-disk electrode (RRDE) voltammetry technique (Figure 3b). When the potential is negatively swept from +1.150 to −0.150 V, the current density of the disk electrode shows a sudden increase for all of the investigated samples due to the emergence of ORR. One may note that the $CoSe_2$ reference sample shows a much negative onset potential and lower current density than $CoSe_2$/GC, and the ORR on it follows a quasi-two-electron pathway (Figure S5a), signifying the importance of the GC framework. Specifically, the onset potentials are determined to be +0.892 V for Cu-14-Co_3Se_4/GC, +0.830 V for $CoSe_2$/GC, and +0.921 V for the commercial Pt/C catalyst, and the corresponding half-wave potentials ($E_{ORR,1/2}$) are observed at +0.782 V for Cu-14-Co_3Se_4/GC, +0.686 V for $CoSe_2$/GC, and +0.823 V for Pt/C. These results suggest that Cu-14-Co_3Se_4/GC has the best ORR catalytic activity among the three cobalt selenide-based samples and is also close to the Pt/C catalyst. Note that this is the first report on the observation of effective ORR activity for Co_3Se_4 composites.

From the series RRDE voltammograms depicted in Figure 3c, one can find that the limiting currents for the Cu-14-Co_3Se_4/GC modified electrode substantially increase with the rotation speed, increasing from 225 to 2500 rpm, and the corresponding Koutecky−Levich (K−L) plots display good linearity with a nearly consistent slope, indicating that the sample shows a quasi-first-order ORR reaction kinetics, that is, the reaction rate is proportional to the oxygen concentration in the solution.[36] The correlated Tafel plots are shown in Figure 3d, where a Tafel slope of only 56 mV dec^{-1} was determined for Cu-14-Co_3Se_4/GC, which is much lower than the 101 mV dec^{-1} for $CoSe_2$/GC, 95 mV dec^{-1} for $CoSe_2$, and even the 88 mV dec^{-1} for Pt/C, suggesting the considerable catalytic activity for ORR on Cu-14-Co_3Se_4/GC, and the involved reaction mechanism is changed from Temkin-type adsorption to Langmuir adsorption condition upon Cu(II)-ion-doping-induced structural transformation.[37]

The number of electron transfer (n) and the H_2O_2 yield for the investigated samples were also calculated (Figure S5a), and distinct changes can be found after structural transformation as depicted in Figure 3e; the n values for Cu-14-Co_3Se_4/GC are higher than that of $CoSe_2$/GC within a wide potential range from 0.00 to 0.75 V. For example, the n value at +0.700 V is determined to be 3.75 for Cu-14-Co_3Se_4/GC, which is higher than that of $CoSe_2$/GC (3.58). Besides, the H_2O_2 yield at +0.700 V is calculated to be 12.16% for Cu-14-Co_3Se_4/GC, which is significantly lower than the 22.24% for $CoSe_2$/GC. These results suggest that the resulting Cu-14-Co_3Se_4/GC shows an obvious higher selectivity toward $4e^-$ reduction[36] of oxygen and a lower byproduct yield compared with $CoSe_2$/GC. Taking the above observations into account, it is obvious that the Cu(II)-ion-doping-induced structural transformation contributes to a remarkable enhancement in ORR catalysis from all aspects. Moreover, Cu-14-Co_3Se_4/GC shows an outstanding operation stability, which is higher than Pt/C. As shown in Figure 3f, after continuously working for 30 000 s, although partial Co_3Se_4 was converted to $Co(OH)_2$[38−40] (Figures S6 and S7), the Cu-14-Co_3Se_4/GC catalyst can maintain 94.0% of its initial voltammetry current, while the voltammetry current of Pt/C decreased to 76.2% of its initial value.

Note that the M-N_x-C_y species are usually considered as the active sites for ORR on Co−N/C catalysts prepared at high temperatures (mostly 600−1000 °C).[39,41,42] However, the cobalt selenide composites with hybrid carbons in the present work were prepared at a temperature no higher than 300 °C. Thus, M-N_x-C_y species are lacking, and it is obvious that the ORR activity for Cu-14-Co_3Se_4/GC results from other species. First, the nonstoichiometric Co_3Se_4 itself may play a significant role in the remarkable enhancement of ORR catalytic activity[14,22] due to the presence of the intrinsically catalytic active Co^{3+} species that can benefit the adsorption of oxygen for electrocatalysis.[14,43,44] Second, the high electrical conductivity of hybrid carbon networks may facilitate charge transfer, while the high surface area comprising abundant hierarchical mesopores may maximize the exposure of active sites and promote mass diffusion. Hence, one can conclude that the evident ORR performance of the Cu-14-Co_3Se_4/GC sample most likely results from the synergistic effects of active nonstoichiometric cobalt selenide and the conductive carbon hybrid networks.[14,22,39]

The Cu-14-Co_3Se_4/GC sample also showed evident OER activity in the 1.0 M KOH solution. As for the LSV curves in Figure 4a, the voltammetry currents underwent an abrupt increase when the potential was gradually increased from +1.050 to +1.700 V, indicative of an obvious OER catalytic activity. Specifically, a potential of only +1.510 V (i.e., $E_{OER,10}$) was required to reach a current density of 10 mA cm^{-2}, which is much lower than that of $CoSe_2$/GC (+1.570 V), $CoSe_2$ (+1.600 V), and even the commercial RuO_2 catalyst (+1.540 V), signifying that the OER activity of Cu-14-Co_3Se_4/GC is superior to that of $CoSe_2$/GC, $CoSe_2$, and also the benchmark RuO_2 catalyst. Moreover, after continuously running for 12 000 s, although Co atoms are converted to cobalt hydroxide and Se atoms are leached (Figure S8),[44,45] the Cu-14-Co_3Se_4/GC sample is able to show a current retention of 83.1% (upper panel in Figure 4g). In contrast, the RuO_2 catalyst can only retain 61.9% of its initial current, indicative of a high OER operation stability for Cu-14-Co_3Se_4/GC.

From the corresponding Tafel plots depicted in Figure 4b, a slope of 111 mV dec^{-1} was determined for Cu-14-Co_3Se_4/GC, which is lower than that of $CoSe_2$/GC (128 mV dec^{-1}) and $CoSe_2$ (221 mV dec^{-1}) and close to that of RuO_2 (82 mV dec^{-1}), indicating that after structural transformation, the resulting Cu-14-Co_3Se_4/GC showed an improved OER kinetics and enhanced bubble-releasing ability. Besides, the electrochemical impedance spectra (upper panel in Figure 4f) revealed that Cu-14-Co_3Se_4/GC displayed a smaller semicircle than $CoSe_2$/GC, $CoSe_2$, and even RuO_2, signifying that OER proceeded on Cu-14-Co_3Se_4/GC required the lowest activation energy among all of the investigated samples in the present work.[24] The excellent OER catalytic performance of Cu-14-Co_3Se_4/GC is mainly attributed to the intrinsically highly active OER species Co_3Se_4[14,22] because of the presence of mixed valences of Co^{2+} and Co^{3+}.[14,22,23]

The voltage difference (ΔE) between $E_{OER,10}$ and $E_{ORR,1/2}$ is a key factor for assessing the activity of oxygen reversible electrocatalysis in the same working electrolyte, where a smaller ΔE suggests a lower efficiency loss and a better activity for catalysts utilized as reversible oxygen electrodes.[14] From the linear sweep voltammograms depicted in Figure 4c, a ΔE of only +0.680 V is observed for Cu-14-Co_3Se_4/GC in 1.0 M KOH aqueous solution, which is much lower than the +0.800 V for $CoSe_2$/GC and +0.990 V for $CoSe_2$ and comparable to the

DOI: 10.1021/acscatal.9b04060
ACS Catal. 2019, 9, 10761−10772

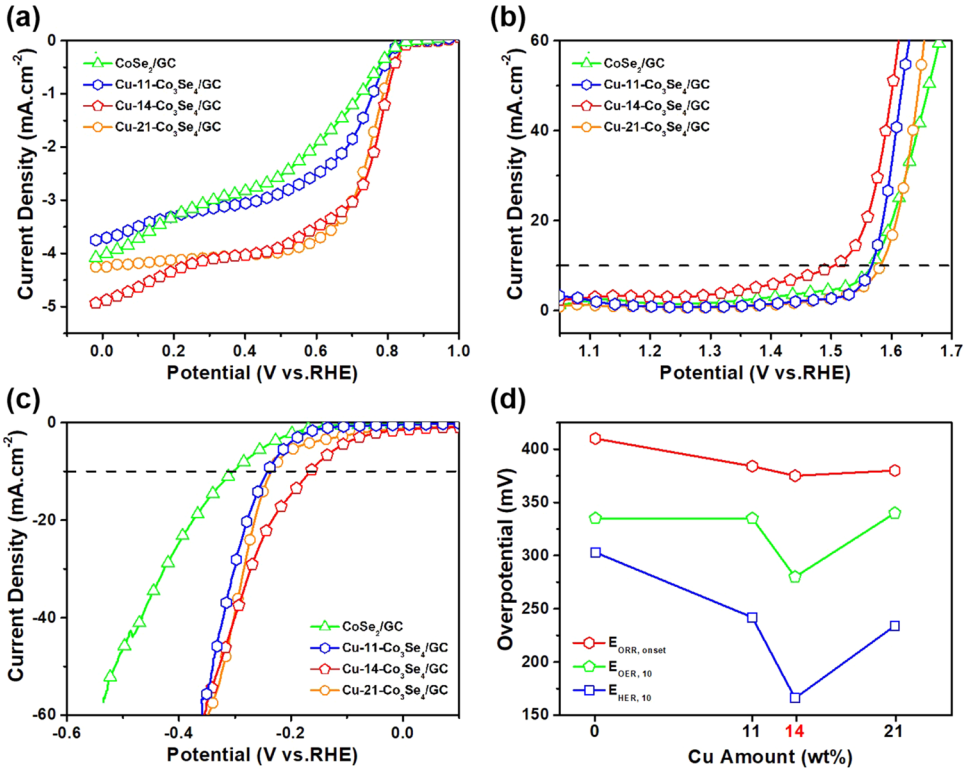

Figure 5. LSV curves of different catalysts catalyzing (a) ORR in 0.1 M KOH at an electrode rotation rate of 1600 rpm; (b) OER and (c) HER in 1.0 M KOH solution at a potential scanning rate of 10 mV s^{-1} after iR correction. (d) Plot showing the variation of E_{onset} for ORR and E_{10} for OER and HER for different samples.

leading nonprecious-metal-based oxygen reversible electrocatalyst in the literature (Table S1).[5,14,24,46] These observations suggest that the Cu(II)-ion-induced structural transformation from o-$CoSe_2$ to m-Co_3Se_4 plays a significant role in remarkably enhancing the oxygen electrocatalysis performance.

Interestingly, Cu-14-Co_3Se_4/GC catalysts concurrently show obvious HER activities in the same electrolyte used for oxygen reversible electrocatalysis, that is, 1.0 M KOH solution. As shown in Figure 4d, when the electrode potential is negatively swept, the current density displays a sudden increase for all of the four investigated samples due to the emergence of HER. Specifically, an overpotential ($E_{HER,10}$) of only 166 mV is required for Cu-14-Co_3Se_4/GC to reach a current density of 10 mA cm^{-2}, much lower than the 303 mV for $CoSe_2$/GC and 381 mV for $CoSe_2$ and close to that of the commercial Pt/C catalyst. These observations suggest the high potential utilization of the Cu-14-Co_3Se_4/GC sample as an active HER electrocatalyst. This conclusion is further supported by the results from Tafel plots and electrochemical impedance spectroscopy measurements. As depicted in Figure 4e, a Tafel slope of 168 mV dec^{-1} is observed for Cu-14-Co_3Se_4/GC, which is smaller than that of $CoSe_2$/GC (180 mV dec^{-1}) and $CoSe_2$ (292 mV dec^{-1}). On the basis of the Butler−Volmer kinetics model, a Tafel slope of 168 mV dec^{-1} (close to 118 mV dec^{-1}) suggests that the discharge reaction $H^+ + e^- \rightarrow H_{ads}$ is the corresponding rate-determining step for Cu-14-Co_3Se_4/GC.[47] Moreover, from the Nyquist plots (bottom panel in Figure 4f) for the catalyst-modified glassy carbon electrode (GCE), one can find that Cu-14-Co_3Se_4/GC demonstrates the smallest semicircle among the series of cobalt selenide composites in this work, indicating that the Cu(II)-ion-induced structural transformation substantially reduces the charge transfer resistance (R_{ct}) for HER, coinciding with the significantly higher HER activity observed for Cu-14-Co_3Se_4/GC than the other two cobalt selenide composite samples.

The HER operation stability of the investigated samples is evaluated by chronoamperometric measurements. After continuously working for 12 000 s, although partial Co_3Se_4 in Cu-14-Co_3Se_4/GC is converted to $Co(OH)_2$ (Figure S9),[48] the Cu-14-Co_3Se_4/GC catalyst is able to retain 81.3% of its initial current, which is far beyond the corresponding value of Pt/C (60.3%) under the same operation conditions (as depicted in the bottom panel of Figure 4g), illustrating that Cu-14-Co_3Se_4/GC exhibits an excellent HER operation stability in alkaline electrolyte solution. More importantly, the HER catalytic activity of Cu-14-Co_3Se_4/GC is superior to all of the nanostructured Co_3Se_4-based catalysts reported in the literature to date (Figure 4h). These results demonstrate that Cu-14-Co_3Se_4/GC is an outstanding HER electrocatalyst, mainly benefiting from the intrinsic high activity of nonstoichiometric cobalt selenides with Co and Se sites serving as electron and proton acceptance sites in HER, respectively.[23]

To further study the potential application of this Cu-14-Co_3Se_4/GC composite in concurrently catalyzing HER and OER, overall water splitting was carried out in a 1.0 M KOH solution where two pieces of carbon cloth loaded with the Cu-14-Co_3Se_4/GC composite were used as the cathode and anode (Figure 4i), respectively. It is observed that the current density starts to increase markedly when the cell bias is higher than 1.300 V and reaches 10 mA cm^{-2} at a cell bias of 1.620 V, corresponding to a combined overpotential (at both the anode and cathode) of only 390 mV for full water splitting. Meanwhile, a lot of bubbles were generated on the surface of both electrodes, indicative of effectively catalyzing both OER and HER simultaneously with a Cu-14-Co_3Se_4/GC catalyst. These results

DOI: 10.1021/acscatal.9b04060
ACS Catal. 2019, 9, 10761−10772

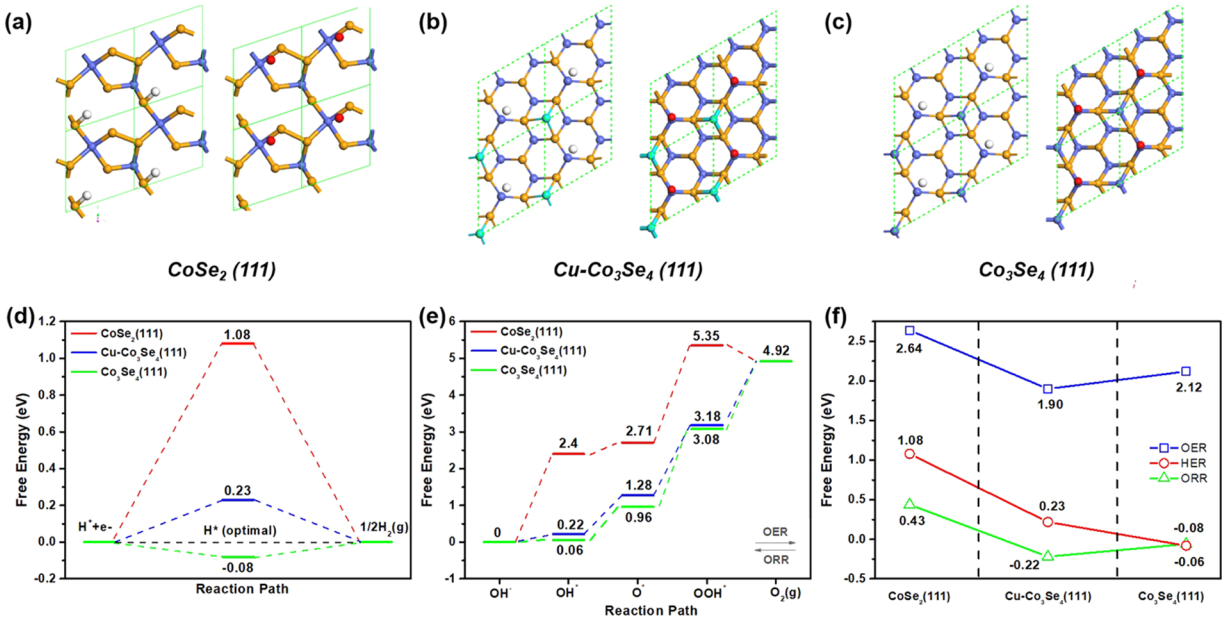

Figure 6. Most stable H* and O* adsorption configurations on the surfaces of (a) $CoSe_2(111)$, (b) $Cu{-}Co_3Se_4(111)$, and (c) $Co_3Se_4(111)$ during HER and OER. Co, Se, and Cu atoms are represented by blue, yellow, and green spheres, respectively. (d) Free energy diagrams for the HER process proceeded on the surface of the $CoSe_2(111)$ plane (red line), the $Cu{-}Co_3Se_4(111)$ plane (blue line), and the $Co_3Se_4(111)$ plane (green line). (e) Free energy diagrams for the OER process (and the reverse process, i.e., ORR) proceeded on the surface of the $CoSe_2(111)$ plane (red line), the $Cu{-}Co_3Se_4(111)$ plane (blue line), and the $Co_3Se_4(111)$ plane (green line). (f) Free energy of the rate-determining steps for HER and OER processes proceeded on the surface of the $CoSe_2(111)$ plane, the $Cu{-}Co_3Se_4(111)$ plane, and the $Co_3Se_4(111)$ plane.

further confirm that structural engineering is an effective way to improve the full water-splitting performance of cobalt selenide-based catalysts.

Comparative studies were also conducted on other control samples prepared with different amounts of Cu salt addition during synthesis to investigate the influence of Cu element content on the corresponding ORR (Figure 5a), OER (Figure 5b), and HER (Figure 5c) electrocatalytic activities of cobalt selenide composites with GC. Figure 5d depicts the key catalytic parameters of different cobalt selenide composites with GC, where one can find that although m-Co_3Se_4 is retained in Cu-21-Co_3Se_4/GC, higher overpotential values are observed for Cu-21-Co_3Se_4/GC as compared with Cu-14-Co_3Se_4/GC. Moreover, the results depicted in Figure 5a–d clearly demonstrate that Cu-14-Co_3Se_4/GC shows the highest trifunctional catalytic activities toward ORR, OER, and HER among the series cobalt selenide samples in the present work, which is probably due to the presence of an optimal balance between the active site density and the surface electronic structure in the Cu-14-Co_3Se_4/GC sample.[27,36] To shed light on the remarkable improvements in electrocatalysis after structural transformation and explore the role of Cu doping in the electrocatalysis process, density functional theory (DFT) calculations were then carried out. Based on the above experimental results, the corresponding interface models were built to describe the interaction between adsorbates and catalyst samples (see the Supporting Information for details). A series of DFT calculation studies suggest that Co atom is the most stable adsorption site for oxygen and hydrogen electrocatalysis no matter whether Cu atoms are incorporated onto the Co–Se skeletons of cobalt selenide or not (Figure S11). In the rate-determining steps, the most stable adsorption configurations for H* and O* on o-$CoSe_2(111)$ and m-$Co_3Se_4(111)$ with and without Cu doping are shown in Figure 6a–c, respectively, and the corresponding Gibbs free energy change ΔG that is considered as a good descriptor of reaction activity was also calculated.

Theoretically, an optimal HER activity can be achieved at $\Delta G_{H^*} \approx 0$.[47,49] As depicted in Figure 6d, the ΔG_{H^*} value on the $Cu{-}Co_3Se_4(111)$ plane is only 0.23 eV, which is much closer to the optimal state, as compared with that on the $CoSe_2(111)$ surface (1.08 eV). This observation clearly signifies that HER on the $Cu{-}Co_3Se_4(111)$ surface is more favorable than that on the $CoSe_2(111)$ plane from the viewpoint of thermodynamics.

As for the $4e^-$ oxygen electrocatalytic mechanism, it is generally believed to proceed via the following steps

$$OH^- + * \leftrightarrow OH^* + e^- \quad (3)$$

$$OH^* + OH^- \leftrightarrow O^* + H_2O(l) + e^- \quad (4)$$

$$O^* + OH^- \leftrightarrow OOH^* + e^- \quad (5)$$

$$OOH^* + OH^- \leftrightarrow O_2 + * + H_2O(l) + e^- \quad (6)$$

where asterisks represent the aforementioned active sites.[2] The OER performance of a catalyst can be evaluated according to the Gibbs free energy change of the rate-determining step, that is, $\Delta G_{OER} = \max(\Delta G_1, \Delta G_2, \Delta G_3, \Delta G_4)$.[50,51] Figure 6e depicts that the step where OOH* forms (eq 5) is the rate-determining step for OER on the $Cu{-}Co_3Se_4(111)$ surface, and thus the ΔG_{OER} is determined to be 1.90 eV. While for OER on the $CoSe_2(111)$ surface, the same rate-determining step is observed, with a much higher ΔG_{OER} of 2.64 eV. Similarly, the ΔG_{ORR} of the rate-determining step on the $Cu{-}Co_3Se_4(111)$ surface (the reverse process of eq 3) is −0.22 eV, while a value of 0.43 eV is observed for the rate-determining step (the reverse process of eq 6) on the $CoSe_2(111)$ surface (Figure 6e), demonstrating that the proceeding of ORR the $Cu{-}Co_3Se_4(111)$ surface is much easier than that on the o-$CoSe_2(111)$ surface. On the basis of these DFT calculation results, one can conclude that Cu–Co_3Se_4 is a more efficient oxygen electrocatalyst than $CoSe_2$.

DOI: 10.1021/acscatal.9b04060
ACS Catal. 2019, 9, 10761−10772

Taking all of the DFT calculation results into account, one can find the positive influence of Cu(II)-ion-induced structural transformation on the reaction mechanisms of hydrogen and oxygen electrocatalysis by lowering the free energy barriers ΔG of the corresponding rate-determining steps (Figure 6f), consistent with the above electrocatalysis results.

CONCLUSIONS

In conclusion, structural transformation from the thermally stable o-$CoSe_2$ to metastable m-phase Co_3Se_4 was performed by adding Cu(II) ions to the precursor. The resulting 3D grape-bunch-like Cu-14-Co_3Se_4/GC sample shows remarkable enhancement in hydrogen/oxygen electrocatalysis. This is the first time that a Co_3Se_4-based remarkable trifunctional electrocatalyst for ORR, OER, and HER has been achieved in the same working electrolyte, featuring an $E_{ORR,1/2}$ of +0.782 V and an $E_{OER,\ 10}$ of +1.510 V, along with an overpotential of 166 mV for HER at 10 mA cm^{-2}, which is also the lowest value among all of the Co_3Se_4-based catalysts reported in the literature. As for oxygen reversible electrocatalysis, it showed a small ΔE of only +0.68 V between the $E_{OER,10}$ and $E_{ORR,1/2}$ as well as an overpotential of only 390 mV for overall water splitting at 10 mA cm^{-2} in 1.0 M KOH aqueous solution. The outstanding catalytic activities for Cu-14-Co_3Se_4/GC were mainly attributed to the catalytically active Co species as well as the highly conductive carbon hybrid networks. DFT calculations further demonstrated that after structural transformation from o-CoSe2 to m-Co3Se4, the Gibbs free energy changes of the rate-determining steps were significantly reduced from 1.08 to 0.23 eV for HER, from 2.64 to 1.90 eV for OER, and from 0.43 to −0.22 eV for ORR electrocatalysis. The results in the present work not only highlight the importance of structural engineering in tailoring electrocatalytic activities but also open up a novel and facile route for structural engineering of transition-metal chalcogenide-based electrocatalysts.

ASSOCIATED CONTENT

Supporting Information

The Supporting Information is available free of charge on the ACS Publications website at DOI: 10.1021/acscatal.9b04060.

Additional experimental data including EDS results, BET results, XPS results, LSV curves, plots of number of electron transfer and peroxide yield, chronoamperometric curves, Tafel plots, electrochemical impedance spectra, and DFT calculations (PDF)

AUTHOR INFORMATION

Corresponding Author

*E-mail: esguili@scut.edu.cn.

ORCID

Zexing Wu: 0000-0002-9059-8688
Chenghao Yang: 0000-0002-3214-328X
Zhiming Cui: 0000-0002-0305-4181
Ligui Li: 0000-0002-1636-9342
Shaowei Chen: 0000-0002-3668-8551

Author Contributions

$^{\bigcirc}$J.D., D.Z., and W.S. contributed equally to this work. The manuscript was written through contributions of all authors. All authors have given approval to the final version of the manuscript.

Notes

The authors declare no competing financial interest.

ACKNOWLEDGMENTS

We gratefully acknowledge the financial support from National Key R&D Program of China (2018YFB1502600), the National Natural Science Foundation of China (NSFC 51402111 and 21528301), the Open Research Fund of State Key Laboratory of Polymer Physics and Chemistry, Changchun Institute of Applied Chemistry, Chinese Academy of Sciences, the Fundamental Research Funds for the Central Universities (SCUT Grant No. 2018 ZD21), and the Research Fund Program of Key Laboratory of Fuel Cell Technology of Guangdong Province.

REFERENCES

(1) Ganesan, P.; Prabu, M.; Sanetuntikul, J.; Shanmugam, S. Cobalt Sulfide Nanoparticles Grown on Nitrogen and Sulfur Codoped Graphene Oxide: An Efficient Electrocatalyst for Oxygen Reduction and Evolution Reactions. *ACS Catal.* **2015**, *5*, 3625−3637.

(2) Wang, N.; Lu, B.; Li, L.; Niu, W.; Tang, Z.; Kang, X.; Chen, S. Graphitic Nitrogen is Responsible for Oxygen Electroreduction on Nitrogen-Doped Carbons in Alkaline Electrolytes: Insights from Activity Attenuation Studies and Theoretical Calculations. *ACS Catal.* **2018**, *8*, 6827−6836.

(3) Jia, Y.; Zhang, L.; Du, A.; Gao, G.; Chen, J.; Yan, X.; Brown, C. L.; Yao, X. Defect Graphene as a Trifunctional Catalyst for Electrochemical Reactions. *Adv. Mater.* **2016**, *28*, 9532−9538.

(4) Peng, X.; Zhang, L.; Chen, Z.; Zhong, L.; Zhao, D.; Chi, X.; Zhao, X.; Li, L.; Lu, X.; Leng, K.; Liu, C.; Liu, W.; Tang, W.; Loh, K. P. Hierarchically Porous Carbon Plates Derived from Wood as Bifunctional ORR/OER Electrodes. *Adv. Mater.* **2019**, *31*, No. e1900341.

(5) Gong, M.; Deng, Z.; Xiao, D.; Han, L.; Zhao, T.; Lu, Y.; Shen, T.; Liu, X.; Lin, R.; Huang, T.; Zhou, G.; Xin, H.; Wang, D. One-Nanometer-Thick Pt_3Ni Bimetallic Alloy Nanowires Advanced Oxygen Reduction Reaction: Integrating Multiple Advantages into One Catalyst. *ACS Catal.* **2019**, *9*, 4488−4494.

(6) Guan, C.; Sumboja, A.; Wu, H.; Ren, W.; Liu, X.; Zhang, H.; Liu, Z.; Cheng, C.; Pennycook, S. J.; Wang, J. Hollow Co_3O_4 Nanosphere Embedded in Carbon Arrays for Stable and Flexible Solid-State Zinc-Air Batteries. *Adv. Mater.* **2017**, *29*, No. 1704117.

(7) Zhang, J. Y.; Wang, H.; Tian, Y.; Yan, Y.; Xue, Q.; He, T.; Liu, H.; Wang, C.; Chen, Y.; Xia, B. Y. Anodic Hydrazine Oxidation Assists Energy-Efficient Hydrogen Evolution over a Bifunctional Cobalt Perselenide Nanosheet Electrode. *Angew. Chem., Int. Ed.* **2018**, *57*, 7649−7653.

(8) Wang, X.; Vasileff, A.; Jiao, Y.; Zheng, Y.; Qiao, S. Z. Electronic and Structural Engineering of Carbon-Based Metal-Free Electrocatalysts for Water Splitting. *Adv. Mater.* **2019**, *31*, No. e1803625.

(9) Zhu, C.; Ma, Y.; Zang, W.; Guan, C.; Liu, X.; Pennycook, S. J.; Wang, J.; Huang, W. Conformal Dispersed Cobalt Nanoparticles in Hollow Carbon Nanotube Arrays for Flexible Zn-Air and Al-Air Batteries. *Chem. Eng. J.* **2019**, *369*, 988−995.

(10) Li, H.; Qian, X.; Zhu, C.; Jiang, X.; Shao, L.; Hou, L. Template Synthesis of $CoSe_2$/Co_3Se_4 Nanotubes: Tuning of Their Crystal Structures for Photovoltaics and Hydrogen Evolution in Alkaline Medium. *J. Mater. Chem. A* **2017**, *5*, 4513−4526.

(11) Xuan, C.; Wang, J.; Xia, W.; Zhu, J.; Peng, Z.; Xia, K.; Xiao, W.; Xin; Huolin, L.; Wang, D. Heteroatom (P, B, or S) Incorporated NiFe-based Nanocubes as Efficient Electrocatalysts for the Oxygen Evolution Reaction. *J. Mater. Chem. A* **2018**, *6*, 7062−7069.

(12) Li, L.; Feng, X.; Nie, Y.; Chen, S.; Shi, F.; Xiong, K.; Ding, W.; Qi, X.; Hu, J.; Wei, Z.; Wan, L.-J.; Xia, M. Insight into the Effect of Oxygen Vacancy Concentration on the Catalytic Performance of MnO_2. *ACS Catal.* **2015**, *5*, 4825−4832.

(13) Ding, W.; Li, L.; Xiong, K.; Wang, Y.; Li, W.; Nie, Y.; Chen, S.; Qi, X.; Wei, Z. Shape Fixing via Salt Recrystallization: A Morphology-

DOI: 10.1021/acscatal.9b04060
ACS Catal. 2019, 9, 10761−10772

Controlled Approach To Convert Nanostructured Polymer to Carbon Nanomaterial as a Highly Active Catalyst for Oxygen Reduction Reaction. *J. Am. Chem. Soc.* **2015**, *137*, 5414−5420.
(14) Meng, T.; Qin, J.; Wang, S.; Zhao, D.; Mao, B.; Cao, M. In Situ Coupling of $Co_{0.85}Se$ and N-Doped Carbon via One-Step Selenization of Metal−Organic Frameworks as a Trifunctional Catalyst for Overall Water Splitting and Zn−Air Batteries. *J. Mater. Chem. A* **2017**, *5*, 7001−7014.
(15) Suntivich, J.; May, K. J.; Gasteiger, H. A.; Goodenough, J. B.; Shao-Horn, Y. A Perovskite Oxide Optimized for Oxygen Evolution Catalysis from Molecular Orbital Principles. *Science* **2011**, *334*, 1383−1385.
(16) Liu, Y.; Cheng, H.; Lyu, M.; Fan, S.; Liu, Q.; Zhang, W.; Zhi, Y.; Wang, C.; Xiao, C.; Wei, S.; Ye, B.; Xie, Y. Low Overpotential in Vacancy-Rich Ultrathin $CoSe_2$ Nanosheets for Water Oxidation. *J. Am. Chem. Soc.* **2014**, *136*, 15670−15675.
(17) Kong, D.; Wang, H.; Lu, Z.; Cui, Y. $CoSe_2$ Nanoparticles Grown on Carbon Fiber Paper: an Efficient and Stable Electrocatalyst for Hydrogen Evolution Reaction. *J. Am. Chem. Soc.* **2014**, *136*, 4897−4900.
(18) Wang, K.; Xi, D.; Zhou, C.; Shi, Z.; Xia, H.; Liu, G.; Qiao, G. $CoSe_2$ Necklace-Like Nanowires Supported by Carbon Fiber Paper: a 3D Integrated Electrode for the Hydrogen Evolution Reaction. *J. Mater. Chem. A* **2015**, *3*, 9415−9420.
(19) McCarthy, C. L.; Downes, C. A.; Schueller, E. C.; Abuyen, K.; Brutchey, R. L. Method for the Solution Deposition of Phase-Pure $CoSe_2$ as an Efficient Hydrogen Evolution Reaction Electrocatalyst. *ACS Energy Lett.* **2016**, *1*, 607−611.
(20) Zhuang, L.; Jia, Y.; Liu, H.; Wang, X.; Hocking, R. K.; Liu, H.; Chen, J.; Ge, L.; Zhang, L.; Li, M.; Dong, C. L.; Huang, Y. C.; Shen, S.; Yang, D.; Zhu, Z.; Yao, X. Defect-Induced Pt-Co-Se Coordinated Sites with Highly Asymmetrical Electronic Distribution for Boosting Oxygen-Involving Electrocatalysis. *Adv. Mater.* **2019**, *31*, No. e1805581.
(21) Li, Y.; Li, F.-M.; Meng, X.-Y.; Li, S.-N.; Zeng, J.-H.; Chen, Y. Ultrathin Co_3O_4 Nanomeshes for the Oxygen Evolution Reaction. *ACS Catal.* **2018**, *8*, 1913−1920.
(22) Hou, Y.; Lohe, M. R.; Zhang, J.; Liu, S.; Zhuang, X.; Feng, X. Vertically Oriented Cobalt Selenide/NiFe Layered-Double-Hydroxide Nanosheets Supported on Exfoliated Graphene Foil: an Efficient 3D Electrode for Overall Water Splitting. *Energy Environ. Sci.* **2016**, *9*, 478−483.
(23) Li, W.; Gao, X.; Xiong, D.; Wei, F.; Song, W.-G.; Xu, J.; Liu, L. Hydrothermal Synthesis of Monolithic Co_3Se_4 Nanowire Electrodes for Oxygen Evolution and Overall Water Splitting with High Efficiency and Extraordinary Catalytic Stability. *Adv. Energy Mater.* **2017**, *7*, No. 1602579.
(24) Wang, N.; Li, L.; Zhao, D.; Kang, X.; Tang, Z.; Chen, S. Graphene Composites with Cobalt Sulfide: Efficient Trifunctional Electrocatalysts for Oxygen Reversible Catalysis and Hydrogen Production in the Same Electrolyte. *Small* **2017**, *13*, No. 1701025.
(25) Luo, Z.; Ouyang, Y.; Zhang, H.; Xiao, M.; Ge, J.; Jiang, Z.; Wang, J.; Tang, D.; Cao, X.; Liu, C.; Xing, W. Chemically Activating MoS_2 via Spontaneous Atomic Palladium Interfacial Doping towards Efficient Hydrogen Evolution. *Nat. Commun.* **2018**, *9*, No. 2120.
(26) Zhao, S.; Huang, J.; Liu, Y.; Shen, J.; Wang, H.; Yang, X.; Zhu, Y.; Li, C. Multimetallic Ni−Mo/Cu Nanowires as Nonprecious and Efficient Full Water Splitting Catalyst. *J. Mater. Chem. A* **2017**, *5*, 4207−4214.
(27) Liu, P.; Hu, Y.; Liu, X.; Wang, T.; Xi, P.; Xi, S.; Gao, D.; Wang, J. Cu and Co Nanoparticle-Co-Decorated N-Doped Graphene Nanosheets: a High Efficiency Bifunctional Electrocatalyst for Rechargeable Zn−Air Batteries. *J. Mater. Chem. A* **2019**, *7*, 12851−12858.
(28) Bose, R.; Patil, B.; Rajendiran Jothi, V.; Kim, T.-H.; Arunkumar, P.; Ahn, H.; Yi, S. C. Co_3Se_4 Nanosheets Embedded on N-CNT as an Efficient Electroactive Material for Hydrogen Evolution and Supercapacitor Applications. *J. Ind. Eng. Chem.* **2018**, *65*, 62−71.
(29) Qiu, B.; Wang, C.; Zhang, N.; Cai, L.; Xiong, Y.; Chai, Y. CeO_2-Induced Interfacial Co^{2+} Octahedral Sites and Oxygen Vacancies for Water Oxidation. *ACS Catal.* **2019**, *9*, 6484−6490.
(30) Zhao, Y.; Jin, B.; Zheng, Y.; Jin, H.; Jiao, Y.; Qiao, S. Z. Charge State Manipulation of Cobalt Selenide Catalyst for Overall Seawater Electrolysis. *Adv. Energy Mater.* **2018**, *8*, No. 1801926.
(31) Zhu, X.; Chong, J.; Hu, T.; Wang, X.; Tian, Y. Enhanced Stability and Metallic Modification of Polymeric and Carbonaceous Nanospheres through Precursor Engineering via a One-Pot Aqueous Strategy Assisted by Iron Ions. *J. Mater. Chem. A* **2017**, *5*, 8297−8306.
(32) Zhu, X.; Wang, S.; Huang, W.; Tian, Y.; Wang, X. Controllable Synthesis of Mesoporous Carbon Nanospheres with Uniform Size by a Facile One-Pot Aqueous Strategy under Highly Acidic Conditions. *Carbon* **2016**, *105*, 521−528.
(33) Li, B. Q.; Zhang, S. Y.; Chen, X.; Chen, C. Y.; Xia, Z. J.; Zhang, Q. One-Pot Synthesis of Framework Porphyrin Materials and Their Applications in Bifunctional Oxygen Electrocatalysis. *Adv. Funct. Mater.* **2019**, No. 1901301.
(34) Xu, N.; Zhang, Y.; Zhang, T.; Liu, Y.; Qiao, J. Efficient Quantum Dots Anchored Nanocomposite for Highly Active ORR/OER Electrocatalyst of Advanced Metal−Air Batteries. *Nano Energy* **2019**, *57*, 176−185.
(35) Li, J.; Liu, H.; Wang, M.; Lin, C.; Yang, W.; Meng, J.; Xu, Y.; Owusu, K. A.; Jiang, B.; Chen, C.; Fan, D.; Zhou, L.; Mai, L. Boosting Oxygen Reduction Activity with Low-Temperature Derived High-Loading Atomic Cobalt on Nitrogen-Doped Graphene for Efficient Zn-Air Batteries. *Chem. Commun.* **2019**, *55*, 334−337.
(36) Niu, W.; Li, L.; Liu, X.; Wang, N.; Liu, J.; Zhou, W.; Tang, Z.; Chen, S. Mesoporous N-Doped Carbons Prepared with Thermally Removable Nanoparticle Templates: an Efficient Electrocatalyst for Oxygen Reduction Reaction. *J. Am. Chem. Soc.* **2015**, *137*, 5555−5562.
(37) Jahan, M.; Liu, Z.; Loh, K. P. A Graphene Oxide and Copper-Centered Metal Organic Framework Composite as a Tri-Functional Catalyst for HER, OER, and ORR. *Adv. Funct. Mater.* **2013**, *23*, 5363−5372.
(38) Pei, Z.; Huang, Y.; Tang, Z.; Ma, L.; Liu, Z.; Xue, Q.; Wang, Z.; Li, H.; Chen, Y.; Zhi, C. Enabling Highly Efficient, Flexible and Rechargeable Quasi-Solid-State Zn-Air Batteries via Catalyst Engineering and Electrolyte Functionalization. *Energy Storage Mater.* **2019**, *20*, 234−242.
(39) Liang, Y.; Li, Y.; Wang, H.; Zhou, J.; Wang, J.; Regier, T.; Dai, H. Co_3O_4 Nanocrystals on Graphene as a Synergistic Catalyst for Oxygen Reduction Reaction. *Nat. Mater.* **2011**, *10*, 780−786.
(40) Sayeed, M. A.; O'Mullane, A. P. A Multifunctional Gold Doped $Co(OH)_2$ Electrocatalyst Tailored for Water Oxidation, Oxygen Reduction, Hydrogen Evolution and Glucose Detection. *J. Mater. Chem. A* **2017**, *5*, 23776−23784.
(41) Bezerra, C. W. B.; Zhang, L.; Lee, K.; Liu, H.; Marques, A. L. B.; Marques, E. P.; Wang, H.; Zhang, J. A Review of Fe−N/C and Co−N/C Catalysts for the Oxygen Reduction Reaction. *Electrochim. Acta* **2008**, *53*, 4937−4951.
(42) Jiang, W. J.; Gu, L.; Li, L.; Zhang, Y.; Zhang, X.; Zhang, L. J.; Wang, J. Q.; Hu, J. S.; Wei, Z.; Wan, L. J. Understanding the High Activity of Fe-N-C Electrocatalysts in Oxygen Reduction: Fe/Fe_3C Nanoparticles Boost the Activity of Fe-N_x. *J. Am. Chem. Soc.* **2016**, *138*, 3570−3578.
(43) Han, X.; He, G.; He, Y.; Zhang, J.; Zheng, X.; Li, L.; Zhong, C.; Hu, W.; Deng, Y.; Ma, T.-Y. Engineering Catalytic Active Sites on Cobalt Oxide Surface for Enhanced Oxygen Electrocatalysis. *Adv. Energy Mater.* **2018**, *8*, No. 1702222.
(44) Zhang, X.; Si, C.; Guo, X.; Kong, R.; Qu, F. A $MnCo_2S_4$ Nanowire Array as an Earth-Abundant Electrocatalyst for an Efficient Oxygen Evolution Reaction under Alkaline Conditions. *J. Mater. Chem. A* **2017**, *5*, 17211−17215.
(45) Li, W.; Xiong, D.; Gao, X.; Liu, L. The Oxygen Evolution Reaction Enabled by Transition Metal Phosphide and Chalcogenide Pre-Catalysts with Dynamic Changes. *Chem. Commun.* **2019**, *55*, 8744−8763.

DOI: 10.1021/acscatal.9b04060
ACS Catal. 2019, 9, 10761−10772

(46) Zhang, X.; Liu, R.; Zang, Y.; Liu, G.; Wang, G.; Zhang, Y.; Zhang, H.; Zhao, H. Co/CoO Nanoparticles Immobilized on Co-N-Doped Carbon as Trifunctional Electrocatalysts for Oxygen Reduction, Oxygen Evolution and Hydrogen Evolution Reactions. *Chem. Commun.* **2016**, *52*, 5946−5949.
(47) Zeng, M.; Li, Y. Recent Advances in Heterogeneous Electrocatalysts for the Hydrogen Evolution Reaction. *J. Mater. Chem. A* **2015**, *3*, 14942−14962.
(48) Xue, Z.; Kang, J.; Guo, D.; Zhu, C.; Li, C.; Zhang, X.; Chen, Y. Self-Supported Cobalt Nitride Porous Nanowire Arrays as Bifunctional Electrocatalyst for Overall Water Splitting. *Electrochim. Acta* **2018**, *273*, 229−238.
(49) Guan, C.; Xiao, W.; Wu, H.; Liu, X.; Zang, W.; Zhang, H.; Ding, J.; Feng, Y. P.; Pennycook, S. J.; Wang, J. Hollow Mo-Doped CoP Nanoarrays for Efficient Overall Water Splitting. *Nano Energy* **2018**, *48*, 73−80.
(50) Li, M.; Zhang, L.; Xu, Q.; Niu, J.; Xia, Z. N-Doped Graphene as Catalysts for Oxygen Reduction and Oxygen Evolution Reactions: Theoretical Considerations. *J. Catal.* **2014**, *314*, 66−72.
(51) Friebel, D.; Louie, M. W.; Bajdich, M.; Sanwald, K. E.; Cai, Y.; Wise, A. M.; Cheng, M. J.; Sokaras, D.; Weng, T. C.; Alonso-Mori, R.; Davis, R. C.; Bargar, J. R.; Norskov, J. K.; Nilsson, A.; Bell, A. T. Identification of Highly Active Fe Sites in (Ni,Fe)OOH for Electrocatalytic Water Splitting. *J. Am. Chem. Soc.* **2015**, *137*, 1305−1313.

DOI: 10.1021/acscatal.9b04060
ACS Catal. 2019, 9, 10761−10772